



# Improved Sliding Mode Observer for the Sensorless Control of Permanent Magnet Synchronous Motor

Hucheng He<sup>1</sup> · Jiangbo Gao<sup>1</sup> · Qin Wang<sup>2</sup> · Jiaruo Wang<sup>1</sup> · Heng Zhai<sup>1</sup>

Received: 23 September 2023 / Revised: 4 December 2023 / Accepted: 1 January 2024  
© The Author(s) under exclusive licence to The Korean Institute of Electrical Engineers 2024

## Abstract

The major drawbacks of the conventional sliding mode observer (SMO) are chattering phenomena and limited robustness. These drawbacks affect the estimated rotor position and speed information of the system. To improve the performance of permanent magnet synchronous motor drives, a sensorless control scheme based on an improved SMO control algorithm is proposed in this paper. A new segmented function with dynamic boundary layer variation is designed and integrated into SMO to reduce the chattering. An adaptive law is adopted to alleviate the phase lag and amplitude attenuation caused by low-pass filters. Based on the back electromotive force value, a phase locked loop is utilized to obtain rotor angular and speed information. Comparative experiments and simulations were conducted to validate the effectiveness of both the conventional SMO and the improved SMO. The results show that the improved SMO can weaken the chattering problem and enhances the system's anti-interference ability.

**Keywords** Adaptive Law · Permanent Magnet Synchronous Motor · Senseless control · Sliding Mode Observer

## 1 Introduction

The PMSM has a history spanning 200 years. With the development of the permanent magnet materials, the improvements of the motor control technology and the advancements of the electronic devices, the PMSM entered an area of rapid development [1, 2]. The PMSM attracts attention in the industrial domain thanks to its favorable characteristics, such as high power density, high efficiency, fast dynamics, and rugged structure [3]. The growing demand in the market for high-performance PMSM, driven by the enhancement of its operational reliability and stability, has made it a focal point of research in the scientific community. Direct torque control (DTC) [4] and vector control (VC) [5] are currently the two primary PMSM control technologies.

In general, the PMSM is controlled to achieve constant torque based on the rotor position. However, the position sensor is sensitive to temperature and vibration, which

makes it impossible to install and apply in some special applications. Therefore, a sensorless control method has been developed for control of the motor.

Sensorless control technology becomes an important research area within the PMSM control system, employing motor voltage and current signals to calculate rotor position and speed information. It can be classified into two categories based on sensorless control technology: one suitable for medium and high-speed operation, and the other for low-speed conditions [6]. In the medium and high-speed domain, the fundamental wave model method is used to calculate rotor position and speed information by back-EMF or flux values. The method mainly including inductance estimation, model reference adaptive, extended Kalman filter, sliding mode observer. When the motor speed decreases, the signal-to-noise ratio of the back-EMF signal decreases, and the system is susceptible to external factors. Therefore, the high-frequency signal injection method is more appropriate for low-speed conditions, utilizing motor pole convexity for rotor position and speed estimation.

In [7], a Hybrid Grey Wolf Optimization Algorithm (HWOA) is proposed for automatically tuning the Sliding Mode Direct Torque Control (SMDTC) of Surface-Mounted Permanent Magnet Synchronous Motors (SPMSMs). The algorithm exhibits fast convergence and effectively avoids

✉ Jiangbo Gao  
13572742434@163.com

<sup>1</sup> College of Electrical and Control Engineering, Xi'an University of Science and Technology, Xi'an, China

<sup>2</sup> Xi'an Highway Research Institute Co., Ltd, Xi'an, China

local optima, showcasing the robust advantages of this control method. In [8], a scheme is proposed for extracting the rotor position angle of an interior PMSM using a high frequency signal injection method combined with iterative strategy. Utilizing the discrete rotor position angle obtained in the angle space, the accuracy increase geometrically with the number of iterations. In [9], a precise sensorless control technique is proposed based on the calibration of SMO with better gain and PLL characteristics. This technique responds quickly and with remarkable accuracy. The approach can still perform well in terms of tracking across a wide range of speeds. In [10], a magnetic variable-speed, partially hybrid ship propulsion motor with auxiliary teeth is introduced. The motor's parametric model is established using finite element software. Evolutionary algorithms and response surface methods are employed to optimize electromagnetic torque and reduce torque ripple. In [11], a sensorless control method for PMSM based on fuzzy sliding mode controller (FSMC) and fuzzy sliding mode observer (FSMO) is developed in order to address the inherent chattering issue of conventional SMO. This control method effectively reduces chattering problem, improves system responsiveness, and allows for adaptive parameter adjustments without increasing complexity. In [12], an adaptive filter was developed based on the static error-free tracking properties of a second-order generalized integrator. It can extract the fundamental signal of the back-EMF and suppresses harmonics. In [13], an improved Model Reference Adaptive System (MRAS) method is proposed for sensorless speed control of an Interior Permanent Magnet Synchronous Motor (IPMSM). The method optimizes Proportional-Integral (PI) controller parameters using the Gray Wolf Optimization Algorithm (GWO), resulting in enhanced rotor speed estimation performance. In [14], the fuzzy non-singular fast terminal sliding mode (FNFTSM) controller enhances the system's reaction time and interference immunity, while the adaptive backstepping (AB) controller and feedforward compensation enhance system resilience for a single PMSM. The fuzzy adaptive sliding mode (FASM) controller is introduced to improve torque estimation precision and enhance disturbance observer performance in tension control. In [15], an improved SMO is proposed to suppress chattering and eliminate phase lags. A Load Disturbance Observer (LDO) is added to the system to compensate for expected disturbances and enhance the system's resistance to load disturbances in order to achieve zero phase delay. In [16], an improved model predictive current control (MPCC) scheme is proposed for Permanent Magnet Synchronous Hub Motor (PMSHM) drives. The scheme is used to replace the proportional-integral (PI) speed loop, and the steady-state performance of the system is greatly improved. In [17], in order to enhance the estimation accuracy of the PMSM sensorless control system and effectively reduce chattering in super-twisting algorithm based SMO (STA-SMO), it is recommended to utilize a second-order SMO optimized by

a BP neural network in combination with an enhanced PLL. Experiments results demonstrates the practicality and effectiveness of the second-order SMO. In [18], a coaxial magnetic gear (CMG) with double-layer permanent magnets (PMs) with a spoke structure is proposed to replace the mechanical gearbox in tidal power generation systems. Utilizing the sensitivity of parameters, optimization analysis is performed using response surface methods and multi-objective genetic algorithms. Experimental results validate that the proposed model has low no-load losses and high efficiency.

This paper proposed an improved SMO to reduce the system's inherent high-frequency chattering phenomena based on the aforementioned research. Firstly, a new piecewise function that remains continuous at zero is introduced, which helps alleviate the chattering associated with the sliding mode issue. Secondly, in order to eliminate the issues of phase lag and amplitude attenuation caused by low-pass filters (LPF), the design of compensation link is eliminated, and the control system's structure is optimized. Finally, an adaptive law is implemented to generate a more accurate back-EMF waveform. The control algorithm effectively reduces sliding-mode oscillations, improves the stability and disturbance rejection of the motor in various conditions at medium or high speeds, optimizes the system structure and enhances control performance. Simulation and experimental results show that this improved SMO can effectively reduce motor chattering and enhance the system's anti-interference ability.

## 2 PMSM Modeling

A surface mounted PMSM model is considered in this paper. The current model of the surface mounted PMSM in  $\alpha\beta$  stationary reference frame is shown as follows:

$$\begin{cases} \frac{di_\alpha}{dt} = -\frac{R}{L}i_\alpha - \frac{1}{L}e_\alpha + \frac{1}{L}u_\alpha \\ \frac{di_\beta}{dt} = -\frac{R}{L}i_\beta - \frac{1}{L}e_\beta + \frac{1}{L}u_\beta \end{cases} \quad (1)$$

where  $i_\alpha, i_\beta$  and  $u_\alpha, u_\beta$  are the stator currents and voltages in stationary reference frame, respectively.  $e_\alpha$  and  $e_\beta$  are back-EMF values in stationary reference frame.  $R$  and  $L$  represent the stator resistance and inductance, respectively.

In stationary coordinate system, the back-EMF of PMSM can be represented as

$$\begin{cases} e_\alpha = -\psi_f \omega \sin \theta \\ e_\beta = \psi_f \omega \cos \theta \end{cases} \quad (2)$$

where  $\omega$  is the rotor angular frequency,  $\psi_f$  is the rotor flux linkage,  $\theta$  is the electrical angular of motor.

### 3 Design of Sliding Mode Observer

The sliding-mode control is used to restrict the state variables on the sliding surface by changing the system structure dynamically. It is widely used for nonlinear system control since it is robust against system parameter variations. For the sensorless control of the PMSM, the sliding-mode controller is adopted for use in the observer design and so is named the SMO. Compared with other control methods, the system structure of sliding mode control technology is always in dynamic change, which makes the control system follow the pre-set state trajectory to do high frequency and small amplitude motion under certain characteristics [19].

Sliding mode motion remains unaffected by changes in controlled object parameters or external interference, contributing to its stronger robustness, faster response, and better dynamic performance. In a PMSM control system, the SMO can replace mechanical sensors to estimate rotor angular position and speed.

#### 3.1 Conventional SMO

According to the mathematical model of the motor, the back-EMF information contains the speed information and the rotor angular. The SMO design is based on the back-EMF information of the rebuilt motor. The estimated value of the observer approaches the real value of the motor within the permitted error range when the difference between the estimated value and the actual value approaches zero.

Taking all the structural parameters of the motor constant, the conventional SMO is constructed as follows:

$$\begin{cases} \frac{d\hat{i}_\alpha}{dt} = -\frac{R}{L}\hat{i}_\alpha + \frac{1}{L}u_\alpha - \frac{k}{L}sign(\hat{i}_\alpha - i_\alpha) \\ \frac{d\hat{i}_\beta}{dt} = -\frac{R}{L}\hat{i}_\beta + \frac{1}{L}u_\beta - \frac{k}{L}sign(\hat{i}_\beta - i_\beta) \end{cases} \quad (3)$$

where  $\hat{i}_\alpha$  and  $\hat{i}_\beta$  are the estimated values and  $k$  is the observer gain. A switching function  $sign(s)$  used:

$$sign(s) = \begin{cases} 1, & s > 0 \\ 0, & s = 0 \\ -1, & s < 0 \end{cases} \quad (4)$$

The sliding surface  $s(x)$  is constructed using the current estimation error:

$$s(x) = \begin{cases} \tilde{i}_\alpha = \hat{i}_\alpha - i_\alpha \\ \tilde{i}_\beta = \hat{i}_\beta - i_\beta \end{cases} \quad (5)$$

where  $\tilde{i}_\alpha$  and  $\tilde{i}_\beta$  are the errors between the estimated current and the actual current.

Dynamic estimation error can be obtained by subtracting Eq. (3) from Eq. (1) and substituting the error into  $s(x)$  to obtain:

$$\begin{cases} \frac{d\tilde{i}_\alpha}{dt} = -\frac{R}{L}\tilde{i}_\alpha + \frac{1}{L}e_\alpha - \frac{k}{L}sign(\tilde{i}_\alpha) \\ \frac{d\tilde{i}_\beta}{dt} = -\frac{R}{L}\tilde{i}_\beta + \frac{1}{L}e_\beta - \frac{k}{L}sign(\tilde{i}_\beta) \end{cases} \quad (6)$$

When the sliding mode of the designed control system occurs:

$$\tilde{i}_\alpha = \tilde{i}_\beta = \frac{d\tilde{i}_\alpha}{dt} = \frac{d\tilde{i}_\beta}{dt} = 0 \quad (7)$$

Substitute (7) into (6) to obtained:

$$\begin{cases} e_\alpha = k \cdot sign(\tilde{i}_\alpha) \\ e_\beta = k \cdot sign(\tilde{i}_\beta) \end{cases} \quad (8)$$

The estimated back-EMF results are directly used to calculate the rotor angular position and velocity as described in Eq. (9).

Using the estimated back EMF voltages, the position and velocity of the rotor are calculated from

$$\begin{cases} \hat{\theta}_1 = -\arctan \frac{\hat{e}_\alpha}{\hat{e}_\beta} \\ \omega = \frac{\sqrt{\hat{e}_\alpha^2 + \hat{e}_\beta^2}}{\psi_f} \end{cases} \quad (9)$$

Considering that the LPF will cause amplitude attenuation and phase lag to the calculation results of the control algorithm, the angular information is compensated [20].

The angular of compensation  $\Delta\theta$  is defined as

$$\Delta\theta = \frac{\omega}{\omega_c} \quad (10)$$

where  $\omega_c$  is the cut-off frequency of the LPF.

Figure 1 shows the block diagram of the conventional SMO for a PMSM system.

#### 3.2 Improved SMO

The conventional SMO employs the switching function as its control function. This function is discontinuous close to zero, and the value regularly swings between  $-1, 0$  and  $1$ , which exacerbates the seriousness of the sliding mode observer's high-frequency chattering phenomena. This paper presents a new piecewise function to replace the switching function in improving the phenomena.

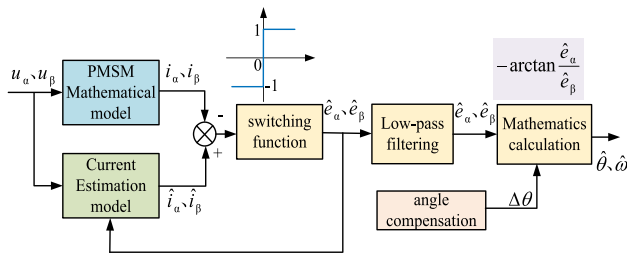


Fig. 1 Block diagram of the conventional SMO

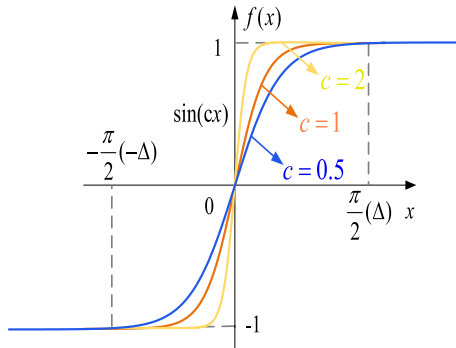


Fig. 2 Variable boundary layers according to the velocity

The new piecewise function is written as

$$f(x) = \begin{cases} 1, & x > \frac{\pi}{2c} \\ \sin cx, & -\frac{\pi}{2c} \leq x \leq \frac{\pi}{2c} \\ -1, & x < -\frac{\pi}{2c} \end{cases} \quad (11)$$

where  $c$  determines the boundary layer width of the function. Figure 2 shows how the boundary layer is changed according to the  $c$ .

In Fig. 2,  $\Delta$  is the boundary layer thickness, and the size of this parameter determines the performance of the SMO. The larger the parameter, the lower the chattering degree, but too large value will lose the rapidity of the system [21]. The function  $f(x)$  is continuous in the domain of definition, showing the characteristics of linear function. In the interval  $x \in (-\infty, -\Delta)$  and  $x \in (\Delta, \infty)$ , the same as the switching function; when  $x = 0$ , the function value is 0. When the  $c$  is small, the function rises slowly; when the  $c$  is larger, the function rises faster. If the function rises too fast at  $x = 0$ , it will be close to the characteristics of the switching function, resulting in a larger system chattering. In generally, this paper takes  $c = 0.5$ .

By using the new piecewise function, the improved SMO is represented as follows:

$$\begin{cases} \frac{d\hat{i}_\alpha}{dt} = -\frac{R}{L}\hat{i}_\alpha + \frac{1}{L}u_\alpha - \frac{k}{L}f(\hat{i}_\alpha - i_\alpha) \\ \frac{d\hat{i}_\beta}{dt} = -\frac{R}{L}\hat{i}_\beta + \frac{1}{L}u_\beta - \frac{k}{L}f(\hat{i}_\beta - i_\beta) \end{cases} \quad (12)$$

The improved SMO equation is obtained by subtracting Eq. (12) from Eq. (1) as follows:

$$\begin{cases} \frac{d\tilde{i}_\alpha}{dt} = -\frac{R}{L}\tilde{i}_\alpha + \frac{1}{L}e_\alpha - \frac{k}{L}f(\tilde{i}_\alpha) \\ \frac{d\tilde{i}_\beta}{dt} = -\frac{R}{L}\tilde{i}_\beta + \frac{1}{L}e_\beta - \frac{k}{L}f(\tilde{i}_\beta) \end{cases} \quad (13)$$

When the sliding mode of the designed control system occurs:

$$\begin{cases} e_\alpha = k \cdot f(\tilde{i}_\alpha) \\ e_\beta = k \cdot f(\tilde{i}_\beta) \end{cases} \quad (14)$$

To identify stable and reachable conditions of the improved SMO, the Lyapunov function can be defined as follows:

$$V = \frac{1}{2}s^T \cdot s \quad (15)$$

where  $s = [s_1, s_2]^T$  represents the sliding surface of the system.

From the Lyapunov stability theorem, the system is asymptotically stable when  $s \cdot s' \leq 0$ , that requirement  $V' \leq 0$ , hence:

$$k > \max \left\{ |e_\alpha|, |e_\beta| \right\} \quad (16)$$

### 3.3 Adaptive Law

The improved SMO can obtain the back-EMF value of the motor. Due to the frequent switching of the inverter and the inherent high frequency phenomenon of the SMO, the observed back-EMF information will contain a large number of high frequency signals. In this paper, the back-EMF adaptive law is introduced to make the observed back-EMF waveform smooth and complete, avoid the use of LPF and the design of phase angular compensation link, and reduce the influence of harmonics on the subsequent processing of the extracted back-EMF signal [22].

Due to the small electrical time constant, the change rate of the motor angular velocity is much smaller than the stator current, and the speed is considered to be constant in a cycle time. Assuming that the motor angular velocity change rate is zero, that is  $\dot{\omega} = 0$ .

The derivative of the PMSM back-EMF shown in Eq. (2) is obtained.

$$\begin{cases} \frac{de_\alpha}{dt} = -\psi_f \cdot \omega \sin \theta - \psi_f \dot{\omega} \sin \theta \\ \quad -\psi_f \omega^2 \cos \theta \\ \frac{de_\beta}{dt} = \psi_f \cdot \omega \cos \theta + \psi_f \dot{\omega} \cos \theta \\ \quad -\psi_f \omega^2 \sin \theta \end{cases} \quad (17)$$

Equation (18) is obtained by substituting  $\dot{\psi}_f = 0$ ,  $\dot{\omega} = 0$  into Eq. (17).

$$\begin{cases} \frac{de_\alpha}{dt} = -\omega \cdot e_\beta \\ \frac{de_\beta}{dt} = \omega \cdot e_\alpha \end{cases} \quad (18)$$

The adaptive law of the back-EMF is designed as follows:

$$\begin{cases} \frac{d\hat{e}_\alpha}{dt} = -\hat{\omega}\hat{e}_\beta - l(\hat{e}_\alpha - e_\alpha) \\ \frac{d\hat{e}_\beta}{dt} = \hat{\omega}\hat{e}_\alpha - l(\hat{e}_\beta - e_\beta) \\ \frac{d\hat{\omega}}{dt} = \tilde{z}_\alpha \hat{e}_\beta - \tilde{z}_\beta \hat{e}_\alpha \end{cases} \quad (19)$$

where  $l$  is the adjustable parameter of the adaptive law of the back-EMF, and the value is a normal number;  $\hat{\omega}$  is the estimated angular velocity value.

The equations of back-EMF errors can be obtained by Eq. (18) from Eq. (19).

$$\begin{cases} \frac{d\tilde{e}_\alpha}{dt} = -\hat{\omega}\hat{e}_\beta + \omega e_\beta - l\tilde{e}_\alpha \\ \frac{d\tilde{e}_\beta}{dt} = \hat{\omega}\hat{e}_\alpha - \omega e_\alpha - l\tilde{e}_\beta \\ \frac{d\tilde{\omega}}{dt} = \tilde{z}_\alpha \hat{e}_\beta - \tilde{z}_\beta \hat{e}_\alpha \end{cases} \quad (20)$$

where  $\tilde{e}_\alpha$  and  $\tilde{e}_\beta$  are the back-EMF errors and  $\tilde{\omega}$  is the angular velocity error.

The error of back-EMF is

$$\begin{cases} \tilde{e}_\alpha = \hat{e}_\alpha - e_\alpha \\ \tilde{e}_\beta = \hat{e}_\beta - e_\beta \end{cases} \quad (21)$$

The angular velocity error is

$$\tilde{\omega} = \hat{\omega} - \omega \quad (22)$$

In order to obtain the stability condition of the adaptive law, the Lyapunov function is defined as

$$V = \frac{(\tilde{z}_\alpha^2 + \tilde{z}_\beta^2 + \tilde{\omega}^2)}{2} \quad (23)$$

Taking the derivative of (5) can be obtained

$$\dot{V} = \tilde{z}_\alpha \dot{\tilde{z}}_\alpha + \tilde{z}_\beta \dot{\tilde{z}}_\beta + \tilde{\omega} \cdot \dot{\tilde{\omega}} \quad (24)$$

Substituting the derivation of Eq. (20) into Eq. (24) and simplifying it, we can obtain

$$\dot{V} = -l(\tilde{z}_\alpha^2 + \tilde{z}_\beta^2) \leq 0 \quad (25)$$

From the Lyapunov stability theorem, the system is asymptotically stable when the parameter satisfied  $l < 0$  for  $\dot{V} < 0$ . The designed adaptive law has asymptotic stability.

### 3.4 Phase-Locked Loop

In the conventional control strategy, the arctangent function is used to estimate the back-EMF value and obtain the rotor angular position. Due to the inclusion of division operation, the chattering and harmonic phenomena of the system are more serious when the  $e_\beta$  value crosses zero.

Phase-locked loop (PLL) is introduced instead of mathematical calculation method in order to avoid the expected deviation of calculation result when the value of back-EMF reaches zero.

Let  $E_{re}$  be the modulus of the back-EMF value, hence:

$$E_{re} = \sqrt{\hat{e}_\alpha^2 + \hat{e}_\beta^2} \quad (26)$$

The angular error signal is constructed as

$$\Delta e = -\hat{e}_\alpha \cos \hat{\theta} - \hat{e}_\beta \sin \hat{\theta} \quad (27)$$

Substitute  $\tilde{z}_\alpha = -k_e \sin \theta$  and  $\tilde{z}_\beta = k_e \cos \theta$  into the Eq. (27) and simplify them to obtain

$$\begin{aligned} \Delta e &= k_e \sin \theta \cos \hat{\theta} - k_e \cos \theta \sin \hat{\theta} \\ &= k_e \sin(\theta - \hat{\theta}) \end{aligned} \quad (28)$$

In Eq. (28), when  $(\theta - \hat{\theta})$  approaches zero, the observed angular value infinitely approaches the actual motor angular, that is,  $\sin(\theta - \hat{\theta}) \approx \theta - \hat{\theta}$ , hence:

$$\Delta e = k_e(\theta - \hat{\theta}) \quad (29)$$

Orthogonal PLL is constructed based on the conventional PLL theory. Figure 3 shows the block diagram of PLL rotor speed and angular estimation.

where  $k_p$  is the proportional gain and  $k_i$  is the integral gain. When the motor speed is stable, the system speed error tends to zero, and the estimated speed is close to the actual speed of the motor.

Figure 4 shows the block diagram of the improved SMO. A segmentation function is employed as the switching function to reduce chattering. Additionally, an adaptive law after the SMO is applied to replace the LPF, which can alleviate phase lag and amplitude attenuation of the back-EMF value. Finally, PLL is used to obtain rotor angular and speed information of PMSM.

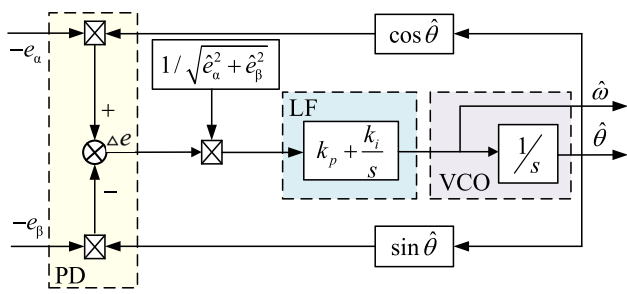


Fig. 3 Block diagram of PLL rotor speed and angular estimation

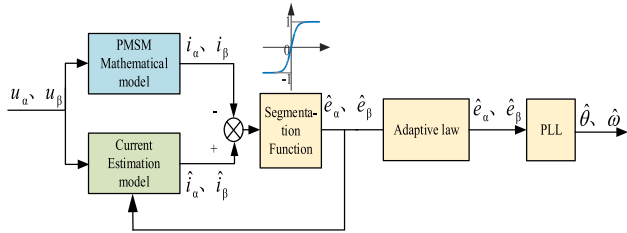


Fig. 4 Block diagram of the improved SMO

Table 1 Simulation parameters of PMSM

Symbol	Parameters	Value/unit
$U$	Rated voltage	220 V
$f$	Rated frequency	50 Hz
$R$	Stator resistance	2.875 $\Omega$
$L_d$	d-axis inductance	8.5e-3 H
$L_q$	q-axis inductance	8.5e-3 H
$\Psi_f$	Flux linkage	0.175 Wb
$J$	Moment of inertia	1e-3 kg·m <sup>2</sup>
$p$	Polar pairs	4

### 4 Simulation Results and Analysis

The control of system designed in this paper used surfaced mounted PMSM, and the simulation parameters of the PMSM are shown in Table 1. A simulation model of PMSM is built based on MATLAB/Simulink software platform to simulate the two working conditions of speed mutation and load mutation. Two kinds of experiments, conventional SMO and improved SMO under the same conditions, were done in this section. By comparing the simulations results, analyze the performance advantages and disadvantages of the two control schemes and ultimately arrive at the corresponding conclusion.

The first working condition is set as: the conventional SMO and the improved SMO were given the initial speed, starts from 1000 r/min, increases to 1500 r/min at 0.06s

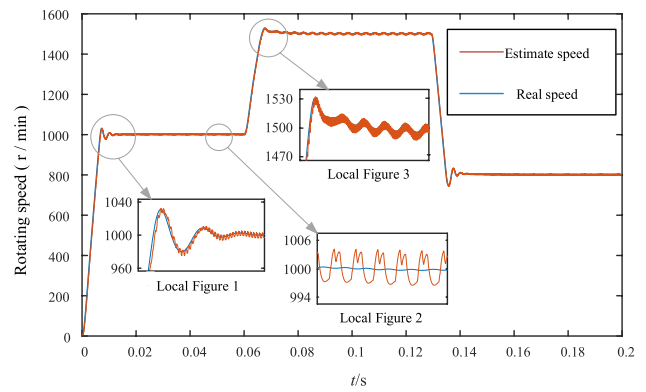


Fig. 5 Speed of conventional SMO

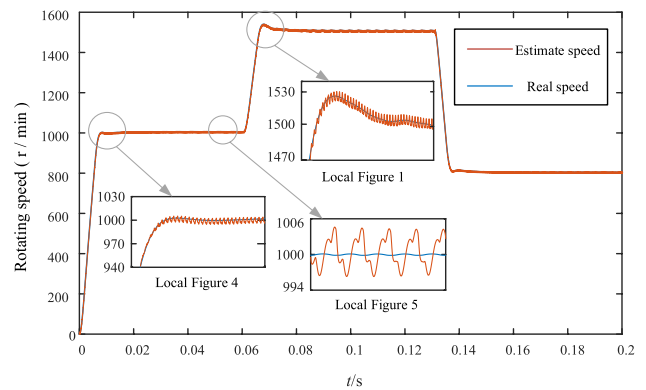


Fig. 6 Speed of improved SMO

and decreases to 800 r/min at 0.14 s, without load added into the system.

Figures 5 and 6 shows the speed of the conventional SMO and improved SMO without load condition. It can be seen the results when the speed increase from 1000 to 1500 r/min until the system reach the stable state and then decreases from 1500 to 800 r/min. From these results, the conventional SMO estimation method has a large overshoot before reaching the stable state, and the fluctuation degree becomes larger with the increase of the given speed, and the improved SMO estimation methods has no overshoot before the speed is stable.

From Figs. 5 and 6, the improved SMO estimation method was made a significant improvement in the overshoot performance compared to the conventional SMO.

Figure 7 shows the speed estimation error of the conventional SMO. It can be seen that during the motor startup phase, the estimation error is about 20 r/min. After the first stabilization, the error remains within 4 r/min. Following a sudden change in speed, the estimation error increases to 15 r/min, and after the second stabilization, it fluctuates around 7 r/min. After the second speed change, the error further increases to 18 r/min. However, after the third

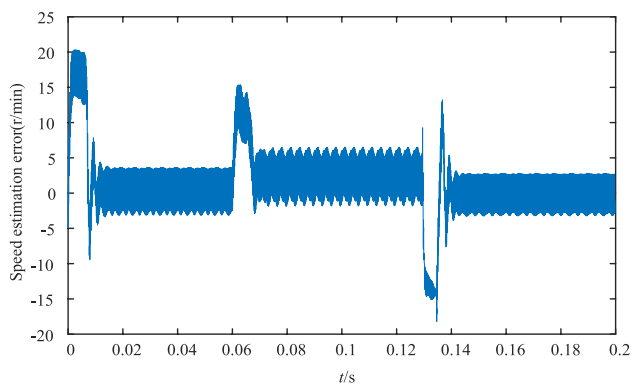


Fig. 7 Speed estimation error of conventional SMO

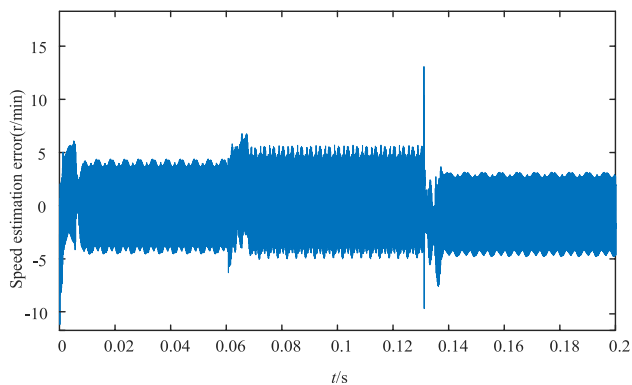


Fig. 8 Speed estimation error of improved SMO

stabilization, the error does not exceed 3 r/min. Therefore, as the speed value increases, the estimation error also increases, and during moments of sudden speed changes, the estimation error is more pronounced. However, it quickly returns to a stable range after a short adjustment period.

Figure 8 shows the speed estimation error of the improved SMO. It can be seen that during the motor startup phase, the estimation error is about 6 r/min. After the first stabilization, the error does not exceed 5 r/min. Following a sudden change in speed, the estimation error increases to 7 r/min, and after the second stabilization, it fluctuates around 5 r/min. After the second speed change, the error further increases to 13 r/min. However, after the third stabilization, the error does not exceed 3 r/min.

From Figs. 7 and 8, the improved SMO estimation method was made a significant improvement in the speed tracking performance compared to the conventional SMO. And the improved SMO exhibits smaller estimation errors during startup, speed variation and stable operation phase.

Figures 9 and 10 shows the angular of the conventional SMO and the improved SMO. By observing the trend of the curves, it can be seen that the both algorithms can effectively track the actual angular variations regardless the motor is

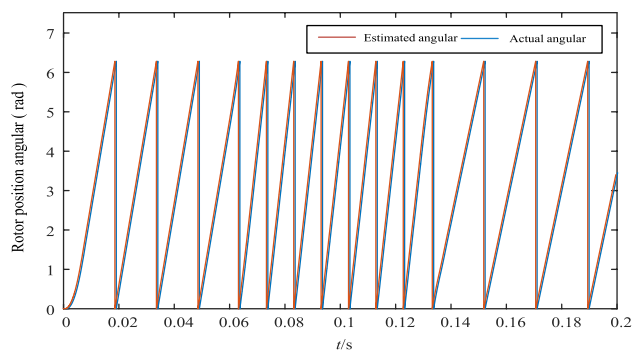


Fig. 9 Angular of conventional SMO

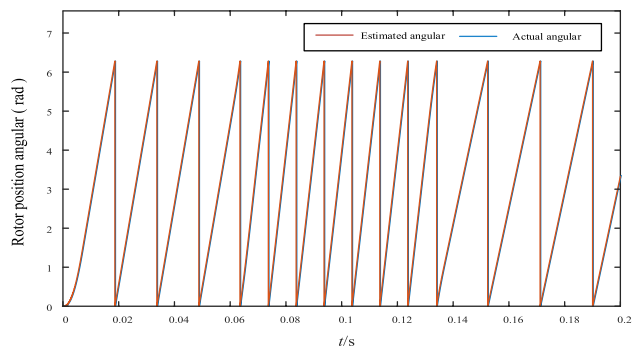


Fig. 10 Angular of improved SMO

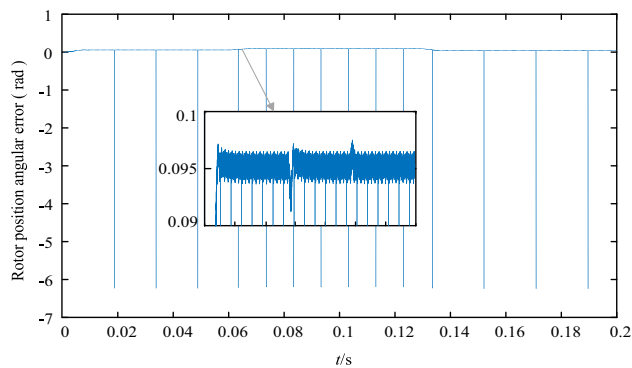
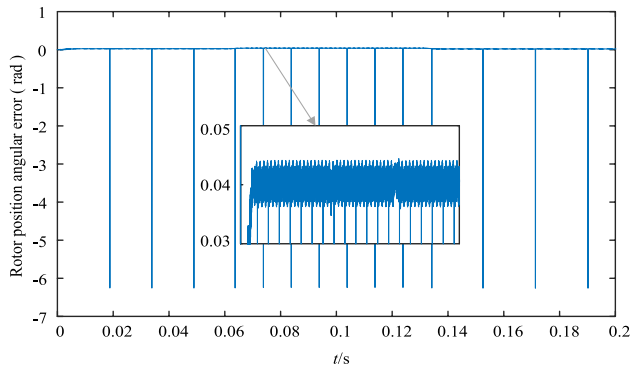


Fig. 11 Angular estimation error of conventional SMO

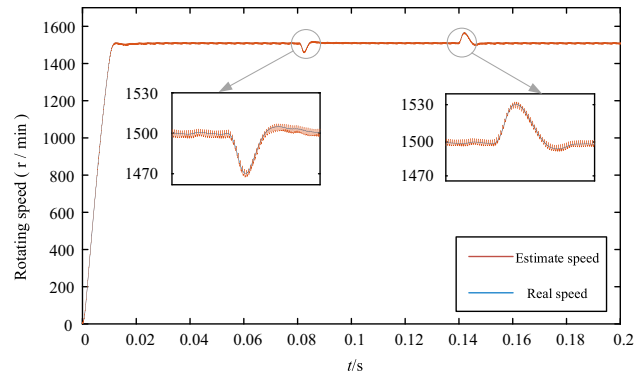
in the startup, stability, speed increases or decreases. The improved SMO demonstrates a higher level of precision in tracking the angular compared to the conventional SMO.

Figure 11 shows the angular estimation error of the conventional SMO. From the graph, it can be seen that the angular estimation error is about 0.095 rad when the system reaches the stable state, and this error slightly increases as the specified speed increases.

Figure 12 shows the angular estimation error of the improved SMO. Form the graph, it can be seen that the



**Fig. 12** Angular estimation error of improved SMO



**Fig. 14** The speed of the improved SMO under load mutation

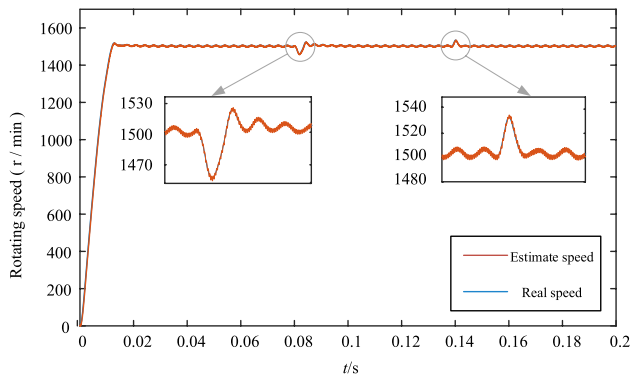


**Fig. 13** The speed of the conventional SMO under load mutation

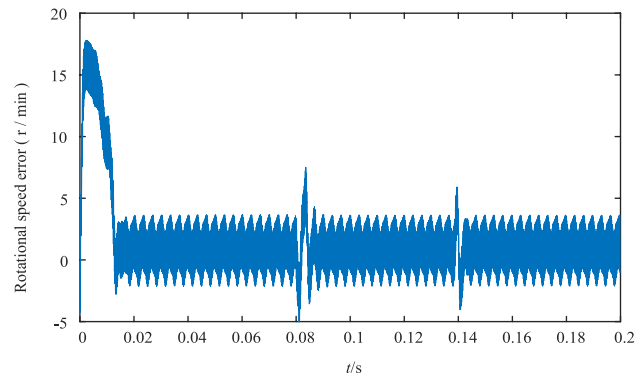


**Fig. 15** The speed estimation error of the conventional SMO under load mutation

angular estimation error is about 0.04 rad when the system reaches the stable state, and this error remains constant as the specified speed increases.

Comparing the curves of Figs. 11 and 12, it is evident that the improved SMO exhibits smaller estimation errors in the rotor angular and superior angular tracking performance compared to the conventional SMO.

The second working condition is set as: the conventional SMO and the improved SMO were given the initial speed, starts from 1500 r/min without load added. After the system stabilizes, a sudden load increases of 10 Nm at 0.08 s and remove the load at 0.14 s.

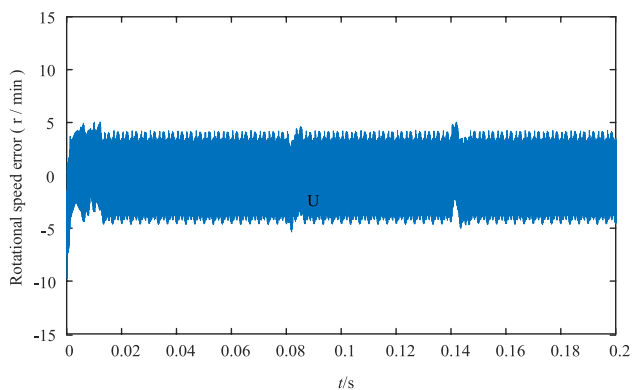
Figure 13 shows the speed of the conventional SMO under load mutation. After the motor starts to enter the stable state, there is obvious speed fluctuation. Following the sudden load increase, the system's speed briefly drops before returning to a steady state. After removing the load, the system's speed briefly increases before settling back into a steady state. During the moments of loading and unloading, the speed fluctuates about 40 r/min, which is 2.7% of the specified speed.

Figure 14 shows the speed of the improved SMO under load mutation. After the motor starts to enter the stable state,

the sudden application of the load causes a brief drop in speed before returning to a steady state. After removing the load, the speed briefly increases before setting back into a steady state. At the moment of loading and unloading, the speed fluctuates about 30 r/min, which is 2% of the specified speed value.

From the Figs. 13 and 14, it can be seen that the fluctuation of the improved SMO decreases under the same conditions, and the anti-load disturbance ability of the system is enhanced.

Figure 15 shows the speed estimation error of the conventional SMO under load mutation. From the figure, it can be seen that the estimation error is about 17 r/min during the motor startup, and the error is less than 4 r/min after the first stability. After the first load mutation, the error is about 8 r/min, and after the second stabilization, the error is about 4 r/min. After the second load mutation, the estimation error is about 6 r/min, and after the third stability, the error does not exceed 4 r/min. When changing the load, the estimation error briefly increases. With control algorithm adjustments, the system can swiftly return to a stable state, demonstrating the system's effective resistance to load disturbances.



**Fig. 16** The speed estimation error of the improved SMO under load mutation

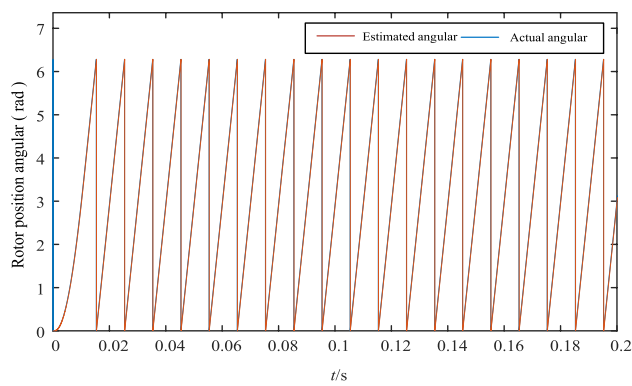


**Fig. 18** The rotor angular of improved SMO under load mutation

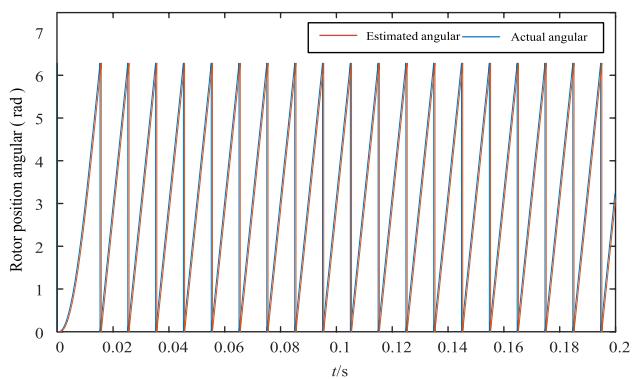


**Fig. 17** The rotor angular of conventional SMO under load mutation

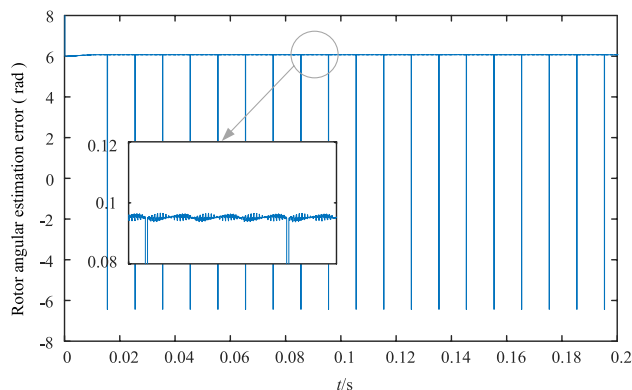


**Fig. 19** The rotor angular estimation error of the conventional SMO under load mutation

Figure 16 shows the speed estimation error of the improved SMO under load mutation. From the figure, it can be seen that the estimation error of the motor start-up, variable load and stable operation stage does not exceed 5 r/min.

Comparing the results shown in Figs. 15 and 16 under the same conditions, the improved SMO has the smaller speed estimation error, and the better speed tracking performance, and the speed tracking performance is not affected by the sudden changes of speed.

Figures 17 and 18 show the rotor angular of the conventional SMO and improved SMO under load mutation. From the figures, it can be seen that when there is a sudden increase or decrease in load, both control algorithms effectively track the actual angular variations.

Figure 19 shows the rotor angular estimation error of the conventional SMO under load mutation. It can be seen from the figure that the rotor angular estimation error is about 0.1 rad.

Figure 20 shows the rotor angular estimation error of the improved SMO under load mutation. It can be seen from the figure that the rotor angular estimation error is 0.04 rad, which is reduced by about 60% compared with the 0.1 rad

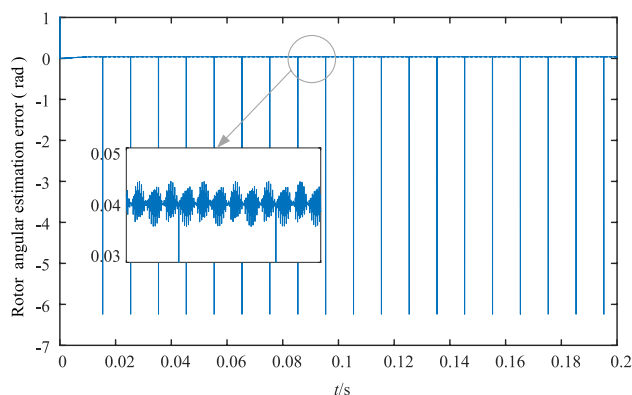


**Fig. 20** The rotor angular estimation error of the improved SMO under Load mutation

estimation error under the conventional SMO. The improved algorithm provides more accurate angular estimation and enhances tracking performance.

Figure 21 shows the back-EMF observation of the conventional SMO. From the figure, it can be seen that during the first cycle of the startup phase, the back-EMF waveform

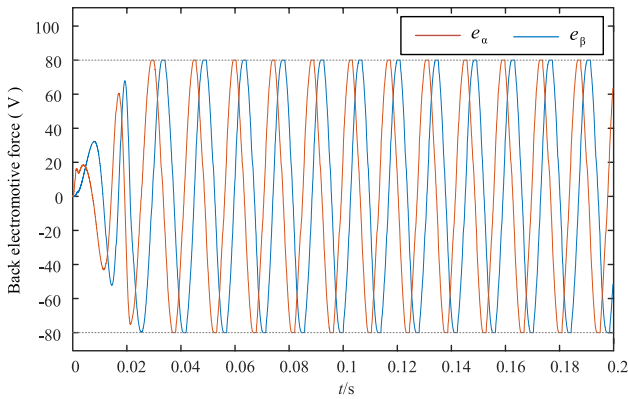


Fig. 21 Back-EMF observation of the conventional SMO

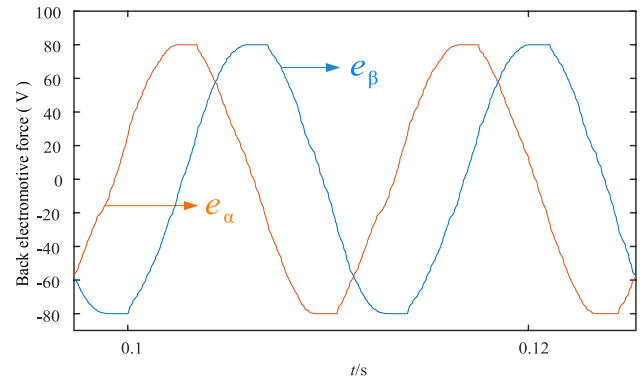


Fig. 23 Local amplification of back-EMF waveform of the conventional SMO

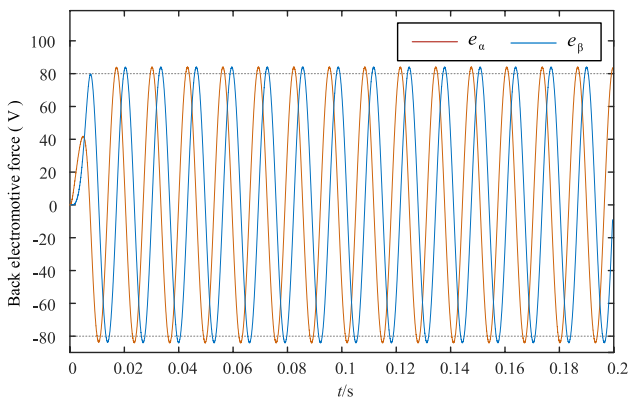


Fig. 22 Back-EMF observation of the improved SMO

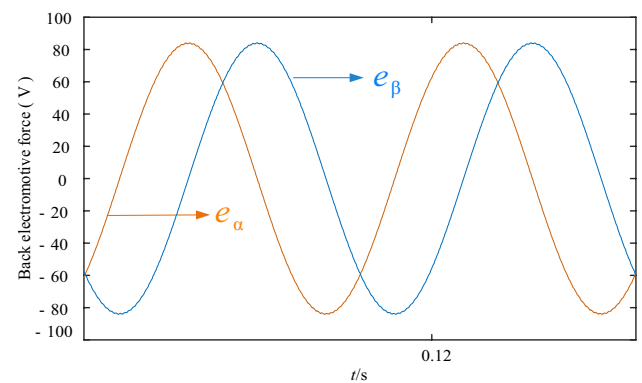


Fig. 24 Local amplification of back-EMF waveform of the improved SMO

exhibits significant distortion, with a double-peak appearance in the  $\alpha$ -axis waveform. It takes about 0.02 s for the system to observe a complete sinusoidal waveform, with a maximum amplitude of about 80 V.

Figure 22 shows the back EMF observation of the improved SMO. It can be seen only in the first half of the cycle during the startup phase, there is a momentary observation inaccuracy in the back EMF signal, and about 0.01 s later, a complete sinusoidal waveform is observed with a maximum amplitude of about 85 V. The removal of low-pass filter in the improved SMO mitigates the issues of signal amplitude attenuation and phase lag in the observed signal.

Figures 23 and 24 show the local amplification of the two back-EMF observation waveforms of the conventional SMO and the improved SMO. The frequent switching of the inverter and the inherent high-frequency characteristics of the SMO result in significant interference in the observed back-EMF. As shown in Fig. 23, the observation waveform of the conventional SMO exhibits poor smoothness, with noticeable distortion at the top and bottom. In contrast, the observation waveform of the improved SMO is more

Table 2 Speed mutation results under two algorithms

	Convention SMO	Improved SMO
Speed fluctuation	Large overshoot	Small overshoot
Speed error	Initial rise followed by stabilization	Extremely small
Angular waveform	Better	Superior
Angular error	Large	Small

complete and smoother, offering a higher level of signal fidelity as shown in Fig. 24.

Tables 2 and 3 respectively show the simulation results of the two algorithms under speed mutation and load mutation conditions. It can be seen that from the overall control effect, the improved SMO improves the rapidity and stability of the system operation to a certain extent. When the speed or load mutation occurs, the improved algorithm has faster adjustment speed and better robustness. Examining the local back-EMF observations, the improved algorithm demonstrates significant improvements in addressing issues

**Table 3** Load mutation results under two algorithms

	Convention SMO	Improved SMO
Speed fluctuation	Large overshoot	Small overshoot
Speed error	Short-term rise followed by stability	Extremely small
Angular waveform	Better	Better
Angular error	Smaller	Accurate
Back-EMF waveform	Distortion at the top and bottom	High fidelity

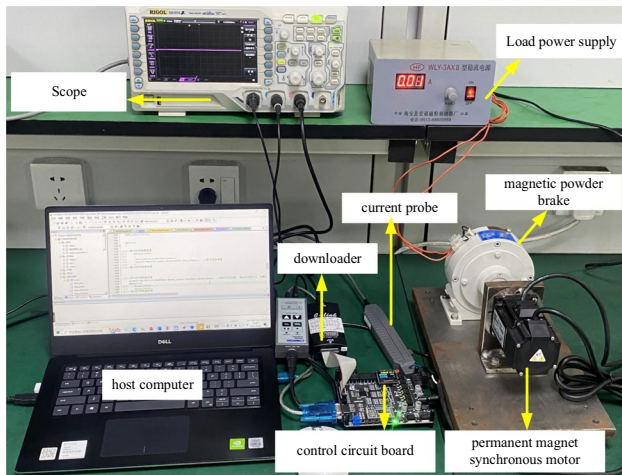


**Fig. 25** Sensorless vector control experimental platform of PMSM

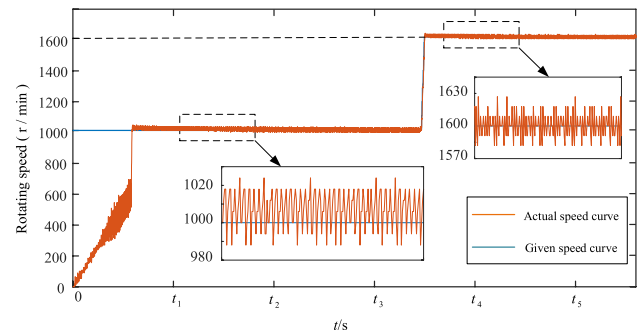
such as amplitude attenuation, phase lag, and observation inaccuracies that are encountered in the conventional SMO.

### 5 Experimental Results and Analysis

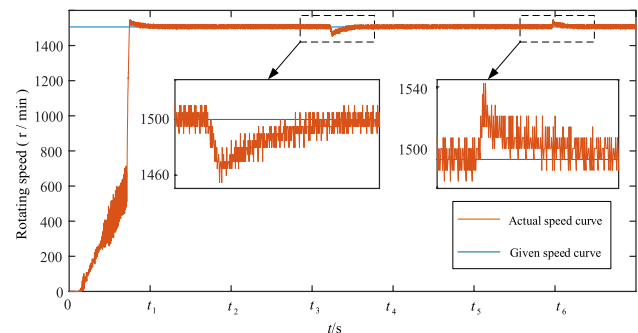
In a laboratory environment, an experimental platform was set up as shown in Fig. 25. The platform utilizes an STM32 development board as the core controller, running a software program to generate PWM signals to control the motor for normal operation.

Figure 26 shows the no-load acceleration experiment waveform of the motor. Initially set at a target speed of 1000 r/min, the speed later ramps up to 1600 r/min after reaching a stable operation. From the figure, it can be seen that while the motor runs steadily at 1000 r/min, the speed fluctuates within the range of 980–1025 r/min, with a variation of about 20 r/min. At 1600 r/min, the speed fluctuates within the range of 1580–1630 r/min, with a variation of about 30 r/min. With the increase of the operating speed, the speed fluctuation increases slightly, but the motor can run well and stably at both given speeds. The control algorithm has good rapidity and stability under no-load variable speed conditions.

Figure 27 shows the experimental waveform under loading and unloading. The motor starts without load, and the



**Fig. 26** No-load acceleration experiment waveform

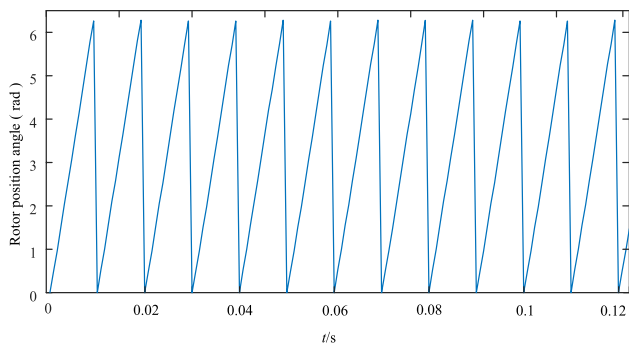


**Fig. 27** The experimental waveform under loading and unloading

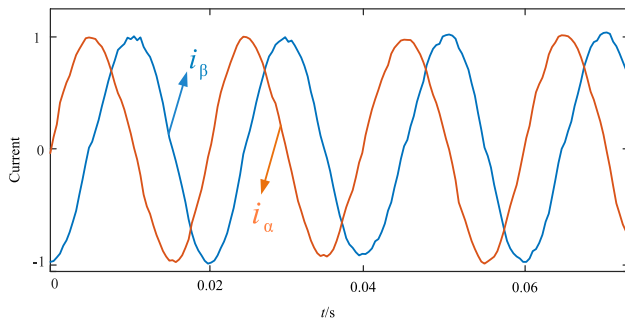
target speed is 1500 r/min. After the first stabilization, a load is applied to the system, and after the second stabilization, the load is removed. From the figure, it can be seen that when a load is applied to the system, the motor’s speed momentarily drops by about 40 r/min. The control system responds immediately and gradually adjusts the speed back to the set value. When the control system runs stably with load, if the load is suddenly removed, the speed rises by about 40 r/min in a short time. The control system also quickly adjusts the speed to return to the target value. The control algorithm has good anti-interference performance.

Figure 28 shows the rotor angular waveform collected when the motor is running stably at 1500 r/min. The waveform is smooth and complete, and has good regularity.

Figure 29 shows the  $\alpha\beta$  axis current waveform collected while the motor operates at 1500 r/min. The sine waveform



**Fig. 28** Rotor angular waveform



**Fig. 29**  $\alpha\beta$ -axis current waveform

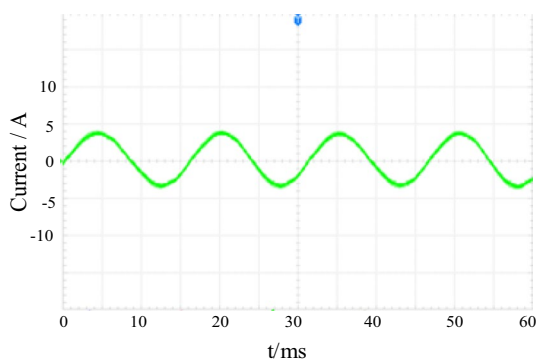


**Fig. 30** A-phase current waveform

is complete and smooth, and only the peaks and troughs of the  $\alpha\beta$ -axis current waveform are slightly flawed.

Figure 30 shows the A-phase current waveform collected while the motor operates at 1500 r/min. The waveform demonstrates good sine and smoothness, indicating stable operation.

Figure 31 shows the A-phase current waveform under loading and unloading. During loading, the current increases rapidly to a stable value, and during unloading, the current decreases rapidly to a stable value. Throughout the loading and unloading processes, there is no significant current

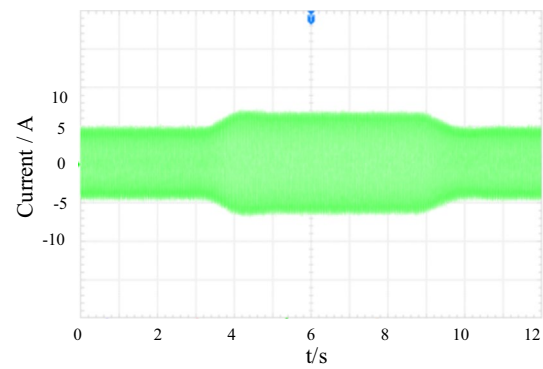


**Fig. 31** A-phase current waveform under loading and unloading

fluctuation, and the changes occur smoothly, reflecting the motor's excellent operational state.

## 6 Conclusion

This paper focus on the serious problem of high-frequency chattering of conventional SMO, the corresponding improved control scheme is proposed. The contributions of this paper can be summarized as follows:

- (1) The mathematical model of SMO is constructed by using a new piecewise function, and the value of relevant parameters is established, which effectively weakens the sliding mode chattering.
- (2) The zero-crossing chattering issue caused by conventional SMO is solved by using a PLL to obtain the speed and rotor position angular, and the extraction accuracy of the reverse EMF is improved by adding adaptive law.
- (3) The simulation and experimental results show that the enhanced control scheme may effectively enhance the motor's stability and disturbance rejection in the medium to high-speed range.

## References

1. Li N, Hao C, Yao Z, Zhang Y (2023) Sensorless control for permanent magnet synchronous motor based on improved sliding mode observer. *Modul Mach Tool Autom Manuf Tech*. <https://doi.org/10.1007/s42835-023-01710-w>
2. Uddin MN, Radwan TS, Rahman MA (2002) Performance of interior permanent magnet motor drive over wide speed range. *IEEE Trans Energy Convers* 17:79–84
3. Shao JB, Wang H, Huang SD, Wu X (2018) A position sensorless control strategy of surface-mounted permanent-magnet synchronous motors for low-speed operation. *Proc CSEE* 38:1534–1541

4. Baader U, Depenbrock M, Gierse G (1992) Direct self control (DSC) of inverter-fed induction machine: a basis for speed control without speed measurement. *IEEE Trans Ind Appl* 28:581–588
5. Wang L, Li JW, Ma Y, Kan HY, Sun BB, Gao S, Wang D (2020) Sensorless control of permanent magnet synchronous motor with improved sliding mode observer. *J Taiyuan Univ Technol* 51:112–117
6. Chi S, Zhang Z, Xu L (2009) Sliding-mode sensorless control of direct-drive PM synchronous motors for washing machine applications. *IEEE Trans Ind Appl* 45:582–590
7. Jin ZJ, Sun XD, Lei G, Guo YG, Zhu JG (2022) Sliding mode direct torque control of spmsms based on a hybrid wolf optimization algorithm. *IEEE Trans Industr Electron* 69:4534–4544
8. Sun XD, Cai F, Yang ZB, Tian X (2022) Finite position control of interior permanent magnet synchronous motors at low speed. *IEEE Trans Power Electron* 37:7729–7738
9. Li XY, Liu JY, Ge LF, Zhong JX, Huang JL, Zhao YC, Song SJ (2023) Sensorless control of the switched reluctance motor based on the sliding-mode observer. *J Electr Eng Technol* 18:981–989
10. Jing LB, Wang T, Tang WZ, Liu W, Qu RH (2023) Characteristic analysis of the magnetic variable speed diesel–electric hybrid motor with auxiliary teeth for ship propulsion. In: *IEEE/ASME transactions on mechatronics*, pp1–11
11. Zou XH, Ding HC, Li JH (2023) Sensorless control strategy of permanent magnet synchronous motor based on fuzzy sliding mode controller and fuzzy sliding mode observer. *J Electr Eng Technol* 18:2355–2369
12. Guo JH, Cao TQ, Lin X, Huang HW, Dai J, Zheng M (2022) Sensorless control of permanent magnet synchronous motor based on improved sliding mode observer. In: *Control Engineering of China*, pp 1–9
13. Sun XD, Zhang Y, Tian X, Cao JH, Zhu JG (2022) Speed sensorless control for ipmsms using a modified mras with gray wolf optimization algorithm. *IEEE Trans Transp Electr* 8:1326–1337
14. He ZH, Yu HS (2022) Fuzzy sliding mode adaptive backstepping control of multiple motors winding system based on disturbance observer. *J Electr Eng Technol* 17:1815–1828
15. Xu YP, Wang C, Yuan WW, Li ZF, Yin ZG (2023) Anti-disturbance position sensorless control of PMSM based on improved sliding mode observer with suppressed chattering and no phase delay. *J Electr Eng Technol* 18:2895–2907
16. Sun XD, Li T, Zhu Z, Lei G, Guo YG, Zhu JG (2021) Speed sensorless model predictive current control based on finite position set for PMSHM drives. *IEEE Trans Transp Electr* 7:2743–2752
17. Wang GQ, Zhang HL (2022) A second-order sliding mode observer optimized by neural network for speed and position estimation of PMSMs. *J Electr Eng Technol* 17:415–423
18. Jing LB, Liu W, Tang WZ, Qu RH (2023) Design and optimization of coaxial magnetic gear with double-layer PMs and spoke structure for tidal power generation. In: *IEEE/ASME transactions on mechatronics*, pp 1–9
19. Wang HR, Yu BM (2022) Sensorless vector control of pmsm based on improved sliding mode observer. In: *Electronic technology & software engineering*, pp. 92–95
20. Wang BG, Li JG (2022) Improved sliding mode observer sensorless control of PMSM. *Mach Des Manuf*, pp 189–192
21. Lv DG, Li ZH (2021) Improved sliding mode observer control of surface mounted permanent magnet synchronous motor. *Electr Mach Control* 25:58–66
22. Qiao Z, Shi T, Wang Y, Yan Y, Xia C, He X (2013) New sliding-mode observer for position sensorless control of permanent-magnet synchronous motor. *IEEE Trans Industr Electron* 60:710–719

**Publisher's Note** Springer Nature remains neutral with regard to jurisdictional claims in published maps and institutional affiliations.

Springer Nature or its licensor (e.g. a society or other partner) holds exclusive rights to this article under a publishing agreement with the author(s) or other rightsholder(s); author self-archiving of the accepted manuscript version of this article is solely governed by the terms of such publishing agreement and applicable law.

**Hucheng He** received the M.S. degree in control theory and control engineering from Xi'an university of science and technology, Xi'an, China, in 2005, and the Ph.D. degree in control science and engineering from Northwestern Polytechnical University, Xi'an, China, in 2008. He is currently a Professor with School of Electrical and Control Engineering, Xi'an University of Science and Technology. His research interests include the power electronics, motor drives, soft switching inverters, analysis of power quality.

**Jiangbo Gao** received the B.S. degree in electrical engineering from the Xi'an University of Science and Technology, Xi'an, China, in 2022. He is currently pursuing the M.S. degree in electrical engineering with the School of Electrical and Control Engineering, Xi'an University of Science and Technology, China. His current research interests include motor drives and control.

**Qin Wang** received the B.S. degree in electrical engineering from the Institute of Disaster Prevention, Hebei, China, in 2019 and received the M.S. degree in electrical engineering from the Xi'an University of Science and Technology, Xi'an, China, in 2023. She is currently an employee of Xi'an Highway Research Institute Co., Ltd. Her research interests include power electronics and motor drives.

**Jiaruo Wang** received the B.S. degree in electrical engineering from the Henan University of Technology, Zhengzhou, China, in 2023. She is currently pursuing the M.S. degree in electrical engineering with the School of Electrical and Control Engineering, Xi'an University of Science and Technology, China. Her current research interests include power electronics and motor drives.

**Heng Zhai** received the B.S. degree in electrical engineering from the Shanxi University of Technology, Hanzhong, China, in 2023. He is currently pursuing the M.S. degree in electrical engineering with the School of Electrical and Control Engineering, Xi'an University of Science and Technology, China. His current research interests include power electronics and motor drives.